The influence of rock heterogeneity on the scaling properties of simulated and natural stylolites

M. Ebner, D. Koehn, R. Toussaint, François Renard

1

2

The influence of rock heterogeneity on the scaling properties of simulated

and natural stylolites

5

6

7   Marcus Ebner*(a), Daniel Koehn (a), Renaud Toussaint (b,c) & François Renard (d)

8

9

10   (a) Tectonophysics, Institute of Geosciences, Johannes Gutenberg University, Becherweg 21,

11   D-55099 Mainz, Germany;

12   (b,c) Institut de Physique du Globe de Strasbourg, UMR CNRS 7516,

13   EOST, Université de Strasbourg I, 5 rue Descartes, F-67084 Strasbourg Cedex, France

14   (d) LGCA-CNRS-Observatoire de Grenoble, Université Joseph Fourier BP 53, F-38041

15   Grenoble, France & Physics of Geological Processes, University of Oslo, Norway

16

17

18   *corresponding author:* ebnerm@uni-mainz.de

19

20

Abstract

Stylolites are among the most prominent deformation patterns in sedimentary rocks that document localized pressure solution. Recent studies revealed that stylolite roughness is characterized by two distinct scaling regimes. The main goal of the present study is to decipher whether this complex scaling behavior of stylolites is caused by the composition of the host rock, *i.e.* heterogeneities in the material, or is governed by inherent processes on respective scales, namely the transition from a surface energy to an elastic energy dominated regime, as theoretically predicted. For this purpose we have developed a discrete numerical technique, based on a lattice spring model, to simulate the competition between stress, strain, and dissolution during stylolite roughening. We varied systematically the quenched noise, initially present in the material, which controls the roughening. We also changed the size, amount, and dissolution rate of the heterogeneities introduced in our model and evaluated the influence on the scaling exponents. Our findings demonstrate that the roughness and growth exponents are independent of the exact nature of the heterogeneities. We discovered two coinciding crossover phenomena in space and time that separate length and timescales for which the roughening process is either balanced by surface and elastic energies. Our observations are coherent with analytical predictions and with investigations quantifying precisely the scaling laws in the morphology of natural stylolites. The findings presented here can further be used to refine volume loss estimates from the finite strain pattern of stylolites.

1. Introduction

Pressure solution in sedimentary rocks results in either intergranular or localized dissolution of material (e.g. Tada & Siever, 1989). The latter is responsible for the formation of stylolites, a frequent deformation pattern in sedimentary rocks (e. g. Stockdale, 1922; Dunnington 1954, Heald, 1955, Park & Schot, 1968, Buxton & Sibley 1981, Rutter, 1983; Railsback, 1993). Stylolites are rough interfaces that frequently contain insoluble material (Fig. 1), which is

2

49 considered to be the residuum of the dissolved rock (Railsback, 1993; and references cited

50 therein). Stylolite initiation is still highly debated (e.g. Tada & Siever, 1989) but several

51 mechanisms have been proposed that are in agreement with field observations: Formation (I)

52 along preexisting anisotropies (Bathurst, 1987) (II) as anticracks (Fletcher and Pollard, 1981)

53 that propagate due to stress concentrations at anticrack tips (even though this idea was

54 challenged recently by Katsman et al. 2006) and (III) by stress induced self-organization

55 (Merino, 1992, Railsback, 1998; Merino et al., 2006).

56 In the present study we focus on a quantitative description and characterization of the

57 roughness of simulated stylolites and study their dynamic development independent of the

58 process leading to the initial development of the localization of dissolution along a plane.

59 Based on recent quantitative methods of stylolite roughness characterization (Renard et al.,

60 2004; Schmittbuhl et al., 2004, Koehn et al., 2007, Ebner et al., submitted) we will use

61 statistical tools to compare simulated and natural stylolites. In particular we study the

62 influence of initial heterogeneity concentration in the host-rock on a) stylolite roughness, b)

63 dynamic roughness growth and c) the correlation of crossover phenomena in space and time.

64 To integrate the results of our study in the context of quantitative characterization we will first

65 review some of the major findings and basic principles, used in recent studies, necessary for

66 the understanding of our approach.

67 The exact classification of stylolites in the field is a difficult task because there is a wide

68 range of geometries (e.g. Park and Schott, 1968) that are often transitional even within a

69 single outcrop. Many previous studies (Park & Schot, 1968; Buxton & Sibley, 1981,

70 Guzzetta, 1984; Tada & Siver, 1989; Railsback, 1993) used classification schemes that were

71 based on visual descriptions of macroscopic features of stylolites. These classification

72 schemes are however not quantitative and hard to compare since these studies focused on a

73 variety of different aspects of stylolite formation. Recent studies, however (Drummond &

74 Sexton, 1998, Karcz & Scholz, 2003) took a more quantitative approach using fractal

75   concepts to describe the stylolite roughness in a statistical sense. They could describe stylolite

76   roughness with a fractal scaling over several orders of magnitude, which means that their

77   roughness is not dominated by a certain wavelength.

78   Renard et al. (2004) and Schmittbuhl et al. (2004) went one step further and revealed that

79   bedding parallel stylolite surfaces show a self-affine scaling invariance with characteristic

80   Hurst exponents (also called roughness exponents). A self-affine rough surface is

81   characterized statistically by the fact that points along the surface separated by a distance Δx

82   from each other are typically distant in the direction transverse to the surface by $\Delta h=\Delta x^{\alpha}$,

83   where α is the roughness exponent. It was further noticed that two distinct scaling regimes

84   exist that were characterized by two different Hurst or roughness exponents separated by a

85   crossover-length (L), around the millimeter scale for the analyzed natural stylolites. Above

86   this crossover, all investigated stylolites exhibit a Hurst exponent of about 0.5 meaning that

87   they change relatively fast from being flat features on larger scale to being rough features on

88   the smaller scale. Below the crossover-length the Hurst exponent is about 1.0, which means

89   that the slopes, or aspect ratio $\Delta z/\Delta x$, stays more or less constant. Schmittbuhl et al. (2004)

90   and Renard et al. (2004) established from first principles of mechanics and chemistry a model

91   for stylolite growth under the form of a stochastic partial differential equation (called in this

92   case a generalized Langevin equation). This equation simulates the roughening of a stylolite

93   surface as a competition between stabilizing forces (that keep the surface flat), which are

94   controlled by long range elastic and local surface tension effects, and destabilizing forces (that

95   roughen the interface) that are induced by pinning effects of material heterogeneities. The

96   analytical solution of Schmittbuhl et al. (2004) reproduced the observed scaling behavior of

97   natural stylolites and demonstrated that the two scaling regimes (characterized by the two

98   different Hurst exponents) correspond to two thermodynamic regimes that are dominated by

99   either surface or elastic energies on small and large scales, respectively (Renard et al., 2004;

100   Schmittbuhl et al., 2004, Gratier et al., 2005). Based on the work of Schmittbuhl et al., (2004)

101   it was demonstrated for the first time by Ebner et al., (submitted) that the crossover-length of

102   natural stylolites, which should be a function of the stress during stylolite growth, can be used

103   to determine stress magnitudes and burial depth in sedimentary basins. The discrete numerical

104   simulation technique of Koehn et al. (2007) enabled to study the dynamics of the roughening

105   process through time revealing that the stylolite interface width w (defined in detail below)

106   grows as a power law with time ($w{\sim}t^{\beta}$) with a growth exponent β of 0.5 in the surface energy

107   dominated regime and a growth exponent of 0.8 in the elastic energy dominated regime. In

108   addition the roughness growth may saturate so that the stylolites lose their memory for

109   compaction or finite strain. It is important to notice that the roughness of simulated stylolites

110   in this contribution is produced by heterogeneities in the material that pin the stylolitic

111   interface due to slower dissolution rate constants, which are in competition with the surface

112   and elastic energies which tend to flatten the surface (Koehn et al., 2007). Therefore the

113   obvious question to ask is whether a variation of the quenched noise changes the scaling

114   properties of the stylolitic interface?

115   Thus, in the present contribution we investigate the influence of different heterogeneities

116   (namely the percentage of pinning particles, their pinning factor (defined below), and their

117   size) on the scaling behavior, dynamic growth, and determined crossover length of simulated

118   stylolites.

119

120   **2. Setup numerical model**

121   The numerical technique that we use to simulate stylolite roughening is based on a lattice-

122   spring model coupled with a dissolution routine (Koehn et al., 2004, 2006, 2007). The model

123   itself is embedded as a module in the *"Elle"* modeling-platform (Bons et al., 2008).

124   For computational reasons, to access large systems and analyze scaling laws over a large ratio

125   between the system size and the resolution, we will consider situations spatially invariant

126   along one of the directions tangential to the stylolite – and effectively treat systems with two

5

127   spatial dimensions. The initial configuration of this 2D model, as shown in Fig. 2a, contains a

128   predefined flat interface that is considered to be filled with a confined fluid. Two blocks of

129   particles are separated by a fluid pocket. Such an approximate configuration would be

130   expected for example, for a fluid pocket embedded between two lowly permeable

131   sedimentary layers. This model system represents two solids or rocks that are pressed together

132   by inward moving top and bottom boundaries, whereas the side boundaries remain fixed

133   (uniaxial strain). A quenched noise (denoted by darker particles in Fig 2a & b) is introduced

134   by a change of the dissolution rate constant of a certain fraction of the particles (= pinning

135   particles) and represents material heterogeneities initially present in the host rock of natural

136   stylolites.

137

138   *2.1. Theory*

139   This section provides only a cursory review on the governing equations of the dissolution

140   process used in the model, for a detailed description and implementation the reader is referred

141   to Koehn et al., (2007) and Bons et al., (2008).

142   The pressure solution process is discretized in steps of dissolution of entire particles,

143   following a linear rate law (Koehn et al., 2007 and references cited therein) according to

144
$$D = kV\left[1 - \exp\left(-\frac{\{\Delta\psi + \Delta\sigma_n\}V}{RT}\right)\right], \qquad (1)$$

145   where D is the dissolution velocity of the interface (m s^{-1}), k a dissolution kinetics rate

146   constant (mol m^{-2} s^{-1}), V the molecular volume of the solid (m^3 mol^{-1}), R the universal gas

147   constant (8.314 J mol^{-1} °K^{-1}), T the temperature (°K), $\Delta\psi$ (Pa) the changes in Helmholtz free

148   energy density (which accounts for the variations in elastic and surface energies) of the solid

149   during dissolution of a solid element, and $\Delta\sigma_n$ (Pa) the differences between the average

150   normal stress along the interface and the local normal stress at a specific location which is due

151   to the repulsion of the solids(Koehn et al., 2007).

152   Surface energies (E^S) of particles are calculated from the local curvature of the interface

153   around each particle, which can be expressed as

154   $$E^s = \frac{\gamma}{\rho},$$ (2)

155   where γ is the surface free energy and ρ is the local radius of curvature of the interface. We

156   consider a plane strain situation, i.e. an invariance along the third spatial dimension, so one

157   radius along the 2D plane investigated entirely characterizes the curvature of the interface –

158   the radius of curvature along the direction of invariance is infinite, and no surface energy is

159   associated to this direction. The surface energies of individual particles are averaged over

160   their neighbors to avoid artifacts from the discreteness of the model (for details see Koehn et

161   al., 2007).

162   In the lattice spring model every particle (i) is connected to its neighbors (j) via a triangular

163   linear elastic spring network. The elastic energy (E^{el}) of a single element is given by

164   $$E^{el} = \frac{1}{4} \sum_{(j)} \kappa \left(\left| x_i - x_j \right| - l \right)^2,$$ (3)

165   where the sum is over all neighbors (j), κ is a spring constant, l is the equilibrium distance

166   between elements i and j.

167

168   *2.2. Basic numerical step*

169   The constitutive equations stated above are implemented as follows:

170   •   Top and bottom walls are moved inwards simultaneously at a given time/deformation

171   step.

172   •   For every deformation step the rate law (Eq. 1) is used to calculate if individual

173   particles at the interface can dissolve in the given time as soon as the two solids meet.

174   •   When elements dissolve they are removed completely and the system can relax.

175   Relaxation is accomplished by an over-relaxation algorithm that finds the new

176   equilibrium configuration for the lattice. Dissolution of particles can take place as long

177   as the given time for the individual deformation step is not consumed.

178   •   If the deformation time is used up or no particles can dissolve within the given time

179   the system is stressed again by a deformation step.

180

181   *2.3. Parameters, boundary conditions, limitations*

182   The material parameters we use resemble those of a limestone, these values are analog to

183   those found in reference works (e.g. Clark, 1966) and in line with values used for the

184   analytical solutions of Renard et al. (2004) and Schmittbuhl et al. (2004): a molar volume of

185   0.00004 m^3/mol, a Young's Modulus of 80 GPa, a Poisson's ratio of 0.33 (this number is

186   given by the triangular lattice configuration), a surface free energy of 0.27 J/m^2, a temperature

187   of 300 K and a dissolution rate constant of 0.0001 mol/(m^2-s). In addition, the displacement

188   rate of the upper and lower boundaries are fixed at a constant value corresponding to

189   velocities between 10^{-10} and 10^{-12} m s^{-1}.

190   The boundary condition can be seen as equivalent to a constant load boundary condition since

191   the dissolution process is fast enough to relax the stresses that build up during a single

192   deformation step. The sidewalls remain fixed during the model runs and there is no wrapping

193   of particles in the x-direction of the model.

194   We use three basic model setups for which we systematically vary the heterogeneities in the

195   structure. All boxes used have the same number of particles (400 particles) in the x-direction

196   but three different particles-sizes were used 0.01 mm, 0.1 mm and 1mm, which corresponds

197   to absolute box-sizes of 4, 40 and 400 mm.

198   To introduce the quenched noise in the simulations a pseudorandom algorithm is used to

199   create a spatial Gaussian distribution of particles that dissolve slower (pinning particles). We

200   varied three parameters of the quenched noise in this study: (i) number of pinning particles in

201   a range from 1-20%, (ii) dissolution rate constant of pinning particles (from 0.1-0.99

202   normalized to the dissolution rate constant of the matrix, which is 1), which determines the

203   pinning factor and (iii) the absolute size of the heterogeneities which varies with the particle

204   size in the range of 0.01-1 mm.

205

206   **3. Data analysis & results**

207   The individual model runs are grouped with respect to the particle-size of the model and are

208   termed *surface*, *intermediate* and *elastic class* according to the dominance of the energy

209   regime during the roughening process. The *surface class* has a particle size of 0.01 mm (box

210   size of 4 mm), the *intermediate class* a particle size of 0.1 mm (box size of 4 cm) and the

211   *elastic class* a particle size of 1mm (box size of 40 cm). In nature the particles may resemble

212   actual grains so that the grain size of the rock varies between the different classes.

213   Unfortunately we are restricted by the resolution of the numerical model to 400 particles in

214   the x-direction, with this resolution a single simulation may run from 10 to 15 days on 4 cores

215   of a recent workstation. Figure 3 shows the roughening of stylolites of these three classes,

216   each with identical quenched noise (5 % pinning particles with half the dissolution rate of the

217   matrix) to demonstrate the influence of the absolute box/particle size. The differences in the

218   roughness and the roughness growth can easily be seen when individual steps of different

219   classes are compared but also by following the growth of individual stylolite peaks along the

220   time axis. In the *elastic class* individual peaks are growing very persistently whereas in the

221   *surface class* the growth is often disrupted, due to dissolution of pinning particles as a result

222   of high surface energies along pronounced peaks.

223   In the following sections we concentrate on the influence of the noise (amount and pinning

224   factor of the noise particles) on 1) the roughness exponents, 2) the growth exponents and 3)

225   the crossover length.

226

227   *3.1. Roughness exponents*

228   To quantitatively characterize the roughness of an individual 1D profile of a stylolite we used

229   concepts from statistical physics (Barabasi & Stanley, 1995), which are briefly introduced in

230   the first part of this section. The methods used here are the same as those of previous studies

231   of natural stylolites (Renard et al., 2004; Schmittbuhl et al., 2004; Gratier et al., 2005; Ebner

232   et al., submitted), which facilitates comparison.

233   The prerequisite for the application of these scaling methods is that the 1D signal of the

234   numerical stylolite obeys a self-affine scaling invariance, which is given by (e.g. Barabasi &

235   Stanley, 1995)

236    $$f(bx) \sim b^{\alpha} f(x), \tag{4}$$

237

238   where *f(x)* is a single valued function and the power-law exponent α is called *roughness* or

239   *Hurst* exponent and provides a quantitative measurement of the roughness of the signal. A

240   self-affine function must be rescaled differently in x and y directions to obtain a scaling

241   invariance i.e. horizontal rescaling of the form *x→bx, b* being a dilation factor, has to be

242   rescaled in the vertical direction by $y \rightarrow b^{-a}y$ to obtain a scaling invariance. Different statistical

243   methods can be used to evaluate the self-affine character of a signal and to determine the

244   associated roughness exponent. We apply two independent methods in this contribution, the

245   *Fourier method* and the *Average Wavelet Coefficient method*.

246   The *Fourier method* (e.g. Barabasi & Stanley, 1995; Schmittbuhl et al., 1995) is based on a

247   Fourier transform of the original 1D signal (Fig. 4a). For every 1D signal (every deformation

248   step) the Fourier power spectrum *P(k)* i.e., the square of the modulus of the Fourier transform,

249   was calculated as a function of the wave-number *k*. Plotting *P(k)* as a function of *k* in log-log

250   space reveals a linear trend for a self-affine function (Fig. 4b),and the slope is a function of

251   the Hurst exponent through (Renard et al., 2004; Schmittbuhl et al., 2004):

252    $$P(k) \sim k^{-1-2\alpha} \quad . \tag{5}$$

253   The *Average wavelet coefficient method* (*AWC*) was used as a second independent method to

254   confirm the scaling results (Simonsen et al., 1998; Hansen et al., 2000). This method is again

255   based on a decomposition of the 1D signal into wavelets, whose amplitude depends on scale

256   and the position. The wavelet transform is defined after Simonsen et al. (1998) by

257
$$W_{a,b} = \frac{1}{\sqrt{a}} \int_{-\infty}^{\infty} \psi\left(\frac{x-b}{a}\right) f(x)dx ,$$
(6)

258   where ψ is the wavelet basis (Daubechies wavelet of order 12) which is parameterized by a

259   scale parameter a and a translation parameter b, and f is the single-valued original function.

260   Finally the wavelet coefficients are averaged over the translation parameter b for every a to

261   obtain the average wavelet coefficient $W(a)$. If the input signal is self-affine, the wavelet

262   transform verifies that the average wavelet coefficient $W(a)$ scales as (Simonsen et al., 1998)

263
$$W(a) \sim a^{\alpha+1/2} .$$
(7)

264   Plotting the average wavelet coefficients as a function of the scale parameter a in log-log

265   space (Fig. 4c), the slope of the linear regression through the data is again a function of the

266   Hurst exponent.

267   Using these two statistical methods, we first study the dynamics of the roughness exponents

268   through time during stylolite growth, and then concentrate on their stability with respect to

269   variations of the noise. The roughness exponents increase relatively quickly in the course of a

270   simulation run (Fig. 4d) and become stable after model step 3000 with only minor

271   fluctuations. The *Fourier*- as well as the *AWC-method* show consistent evolutions and similar

272   values of the roughness exponents. Averages of the plateau values reached (after step 3000)

273   for individual model runs are used as a characteristic value for the roughness exponent for a

274   specific setup. Error bars underline the standard deviation around this average (Fig. 5).

275   The *surface class* is characterized by consistently high values for the Hurst exponent i.e. $\alpha \sim 1$-

276   1.1, independent of the pinning factor (i.e. the dissolution rate constant k in Eq 1; cp Fig. 5a)

277   or the amount of pinning particles (Fig. 5b).

278   The exponents only decrease when the pinning factor of particles is very low (dissolution rate

279   constant > 0.9) and the rock becomes very homogeneous. The most stable roughness

280   exponents for the surface class are reached in the range 0.1 to 0.8 for the pinning factor and 1

281   to 20 % of pinning particles.

282   The *elastic class* reveals lower Hurst exponents ($\alpha\sim$ 0.6 to 0.9) than the *surface class*. If the

283   pinning factor of particles is very strong (below the value 0.4 for the relative dissolution rate

284   constant in Fig. 5a) stress concentrations are locally too high once two pinning particles meet

285   and artifacts develop (usually anticracks that grow laterally emerge from these concentrations,

286   hence modifying the surface topography) in the numerical model within the *elastic class*.

287   Therefore we did not include values below 0.4 from elastic simulations in Fig. 5a. Generally

288   the roughness exponents in the elastic class show stronger fluctuations than those of the

289   surface class. They are relatively stable within a pinning factor range of 0.5 to 0.8 (Fig. 5a)

290   and 1 to 20 % of pinning particles.

291   The *surface* and *elastic classes* correspond well to the two scaling regimes found in natural

292   stylolites (Renard et al., 2004; Schmittbuhl et al., 2004) that are separated by a crossover-

293   length at the millimeter scale. The roughness exponents of the surface class ($\alpha\sim$1.1) are in

294   very good agreement with analytical predictions and experimental observations (e.g. Gratier

295   et al., 2005). The *elastic class* displays values for the Hurst exponent ($\alpha\sim$ 0.6-0.9) that are

296   higher than exponents from natural examples (Renard et al., 2004; Schmittbuhl et al., 2004;

297   Ebner et al., submitted) or analytical predictions, which are generally around 0.5. These

298   analytical predictions are usually based on linear approximations, which are strictly speaking

299   valid as long as the surface morphology is not too developed. The present model does not

300   present any such limitations, and the fully developed situation can thus present a different

301   Hurst exponent from the initial one. The discrepancy with natural data may arise from the

302   large particle (or grain) size that we use in the setup for the elastic class. In nature the grain

303   size is much smaller and corresponds to the values that we use in the surface class.

304

305   *3.2. Interface growth*

306 In addition to the dynamic development of the roughness exponents the simulations allow us

307 to study how fast the amplitude of the stylolite roughness grows through (model-) time or as a

308 function of the finite strain. First we concentrate on different growth regimes of stylolites, the

309 associated growth exponents and prefactors of scaling functions and then study the variation

310 of these factors as a function of host-rock heterogeneities. In order to quantify the amplitude

311 of the roughness we use the *interface width (w)* that is defined as the root-mean-square

312 fluctuation of the height of the interface for a given time-step (Barabasi & Stanley, 1995)

313 $$w(L,t) \equiv \sqrt{\frac{1}{L}\sum_{i=1}^{L}\left[h(i,t)-\bar{h}(t)\right]^2} \ , \qquad (8)$$

314 where *w* is the interface width as a function of system size *L* and time *t*, *h* is the height of

315 point *i* on the interface at time *t* and $\bar{h}$ the average height of the interface at time *t* given by

316 $$\bar{h}(t) \equiv \frac{1}{L}\sum_{i=1}^{L}h(i,t). \qquad (9)$$

317 In our simulations, the system size *L* is defined as the number of elements in the x-direction,

318 which is constant for all simulations, i. e. 400 particles. Roughening processes of interfaces in

319 a wide range of fields have been demonstrated to follow a power law in time (e.g. Barabasi &

320 Stanley, 1995) defined by a growth-exponent β (given by, $w(L,t) \sim t^{\beta}$). This initial phase of

321 interface growth is usually followed by a second regime during which the interface width

322 reaches a saturation value, w_{sat}, which is directly related to the system-size.

323 Both, the growth and saturation regimes can be seen in Fig. 6a for an experiment of the

324 surface class with a characteristic growth exponent of *β~0.5*. The arrow in Figure 6a marks

325 the transition from the power law growth regime to the regime where the interface width

326 saturates and stays constant. The *intermediate class* simulations show a similar growth

327 exponent (around 0.5) but do not saturate in the given deformation time. The *elastic class*

13

328   (Fig. 6b) shows two successive growth regimes, the first being defined by a growth exponent

329   of $\beta \sim 0.5$ up to a crossover interface width followed by a second regime with $\beta \sim 0.8$ without

330   reaching the saturation regime. We suggest the following schematic growth regimes (Fig 6c)

331   for stylolites: (i) growth in the surface energy dominated regime with an exponential growth

332   defined by $\beta \sim 0.5$ followed by (ii) growth in the elastic energy dominated regime with $\beta \sim 0.8$

333   and finally reaching (iii) a saturation regime where the interface width stays constant.

334   This strict non-linearity of the interface growth in our simulations suggests that estimated

335   amounts of compaction (here used as synonymous with volume/area loss due to pressure

336   solution) from stylolite amplitude heights (e.g. Tada & Siever, 1989 and references cited

337   therein) only capture a small part of the actual compaction. To cope with this problem, Koehn

338   et al. (2007) demonstrated that the actual displacement can be expressed for the elastic or

339   surface energy dominated growth regimes as a function of the interface width and the growth

340   exponent (as long as the critical saturation time is not reached), given by

341   $$A \sim (w/l)^{1/\beta} l \qquad\qquad\qquad (10)$$

342   where, A is the compaction displacement, w the interface width, β the growth exponent (for a

343   certain class) and l the particle size. The slope of this function gives a prefactor for the scaling

344   relation which should remain constant until the saturation time is reached. We call the slope

345   of this relation here and in the subsequent sections *compaction prefactor* because it relates the

346   interface width to the total compaction (Fig. 7). As soon as the saturation time is reached the

347   relation does not hold any more and the function deviates from the linear trend (Fig. 7a). This

348   effect can be observed in Figure 7a where the arrow marks the onset of the saturation of the

349   interface width, compaction goes on but the interface width (x-axis) remains constant.

350   However, if the saturation is not attained (Fig. 7b) the actual compaction can be calculated

351   accurately from the interface width and the growth exponent using Eq. 9.

352   Looking at the growth exponent as a function of the quenched noise it can be clearly

353   demonstrated that neither a variation in the pinning factor of particles (Fig. 8a) nor in the

14

354   amount of pinning particles (Fig. 8b) has a significant influence. The values for the growth

355   exponent cluster around $\beta\sim0.5$ for the *surface* and *intermediate classes* and around $\beta\sim0.8$ for

356   the *elastic class*. The compaction prefactors display a higher variability than the growth

357   exponents but no systematic trend can be seen that relates this variation to the pinning factor

358   or amount of pinning particles in the host-rock. Figures 8c & 8d show that there is no

359   significant difference between the three classes of particle sizes used with values for the

360   compaction prefactor in a range between ~12 and ~25. As a third quantity we compare the

361   maximum interface width normalized by the particle size (w_{max}) that develops during

362   simulations with different heterogeneities (Fig. 8e & f). The largest interface widths are

363   achieved in the *elastic class* with $w_{max}\sim20$ in contrast to $w_{max}\sim10$ reached in the *intermediate*

364   and *surface class*. Hence the interface growth displays twice the displacement in the *elastic*

365   *class* in the given simulation time due to the larger growth exponents than those of the

366   *intermediate* or *surface class*, respectively. For the *surface*, *intermediate* and *elastic classes*

367   the variation of the pinning factor of particles (Fig. 8e) have no considerable influence on the

368   maximum interface width. However the amount of pinning particles has a significant

369   influence on the *surface* and *intermediate class* (Fig. 8f). Both classes show an evident

370   decrease in the maximum interface width with increasing amount of pinning particles. This

371   trend cannot be observed in the *elastic class* (Fig. 8f).

372   We also tested the influence of the initial shape of the predefined interface separating the two

373   blocks that are pressed together during an experimental run (compare Fig. 2a), which is flat in

374   all the simulation data shown in the preceding sections. To investigate the dynamic roughness

375   evolution of an already rough interface we arbitrarily choose a time/deformation step (t_n) of a

376   simulation run (Fig 9a) and subtracted the topography (h) of this step from the subsequent

377   time steps similar to $h(t) = h(t_n + m \cdot \Delta t) - h(t_n)$. This procedure allows to investigate the dynamic

378   evolution of a rough interface but statistically evaluating the difference of the evolving

379   roughness from time t_n onwards (Fig 9b). Departing from an already rough interface does not

380   change the scaling parameters (growth and roughness exponent) as depicted in Fig 9. Hence

381   the model setup we choose in this work (i.e. a flat initial interface) can also account for

382   complex initial topographies.

383

384   *3.3. Crossover length scales*

385   The crossover-length of the stylolite roughness that separates the surface energy regime from

386   the elastic energy dominated regime is a function of the stress during stylolite growth and can

387   be used as paleo-stress gauge. It is of fundamental importance to know if this crossover is

388   constant when the heterogeneities in the host-rock vary. In the following section we want to

389   explore how sensitive the crossover-length scale is on variations in the amount and strength of

390   pinning particles. The *surface* and *elastic classes* of our simulations reveal roughness

391   exponents that are characteristic for the two regimes where surface or elastic energy are

392   dominant. The crossover-length between the two regimes can be found in the *intermediate*

393   *class* of our simulations that reveals two different roughness exponents and hence the

394   transition between the two scaling regimes (Fig. 10). The Fourier power spectrum of the 1D

395   signal of a stylolite in the intermediate class (Fig. 10b) shows a change from a shallow to a

396   steep slope, i.e. small and large roughness exponents on large and small scales, respectively.

397   To avoid bias due to improper fitting of the crossover-length we used a nonlinear least square

398   curve fitting algorithm in logarithmic space to model our scaling function (Ebner et al.,

399   submitted)

400    $f(x) = (a_L x + m_L)(1 - w(x)) + (a_S x + m_S)w(x)$ (11a)

401   and

402    $w(x) = \dfrac{(\tanh(x + L) + 1)}{2}$,   (11b)

403   where $a_{L,S}$ are the exponents of the scaling function for large and small scales, $m_{L,S}$ the

404   corresponding intercepts with the ordinate and *w(x)* the weighting function. During this

405   procedure the roughness exponents of our nonlinear model function were fixed according to

406   the roughness exponents ($\alpha_S \sim 1.1$; $\alpha_L \sim 0.5$) reported from natural stylolites (Renard et al., 2004;

407   Schmittbuhl et al., 2004, Ebner et al., submitted).

408   The crossover-lengths obtained for all experiments of the intermediate class are in a range of

409    $L \sim 1.33 \pm 0.09$ mm, the crossover length usually develops simultaneously with the achievement

410   of the plateau values (compare Fig. 4d). Neither of the quenched noise parameters varied in

411   the experiments influences the crossover-length (Fig. 11).

412   The time evolution of the roughness presented in the previous section showed that the surface

413   energy dominated regime is characterized by a growth exponent of 0.5 whereas the elastic

414   energy dominated regime is characterized by a growth exponent of 0.8. Looking at the

415   roughness growth in the elastic class one could still see the slow surface energy dominated

416   growth in the beginning of the roughness evolution (Fig. 6). Therefore the growth exponents

417   also show a transition (that we term the crossover interface width) between growth in the

418   surface energy dominated regime and growth in the elastic energy dominated regime, similar

419   to the two roughness exponents that are characteristic for these two regimes. The crossover

420   interface width is very consistent for all experiments with $w \sim 1.23 \pm 0.04$ mm, independent of

421   the quenched noise introduced in the system. We did not observe a crossover in the interface

422   growth of the *intermediate* and *surface class* because the interface width in these classes is

423   simply not large enough to reach the elastic growth regime. Due to the very good correlation

424   between the magnitudes of the crossover-length and the crossover interface width (Fig. 11)

425   we argue that both crossovers arise from the same process, namely the transition from a

426   surface energy to an elastic energy dominated regime.

427

428   **4. Discussion**

429   In the following section we first discuss the influence of the quenched noise on the scaling

430   parameters in our numerical simulations, deal with the relevance of the noise and compare the

431   results to natural stylolites. Secondly, we will focus on the crossover phenomena and their

432   significance for the estimate of volume loss along a finite natural stylolite.

433   The influence of the exact nature of the heterogeneities (i.e. pinning factor, amount and size

434   of pinning particles) on the scaling exponents can be directly investigated by a close

435   examination of Figures 5, 8 and 11. Doing so, it is immediately evident that the pinning factor

436   has the least influence on the roughness and growth exponents as well as on the crossover

437   scaling (L and w_{cross}), with resulting values that are very consistent over wide ranges of the

438   parameter space. The amount of pinning particles only shows an influence on the maximum

439   interface width w_{max}, which decreases with increasing amount of heterogeneities (Fig. 8f).

440   This fact is in good agreement with observations made on natural stylolites that stylolite

441   amplitudes decrease with the amount of heterogeneities i.e. clay particles (e.g. Tada & Siever,

442   1989, and references cited therein). The scaling exponents themselves are independent of the

443   amount of pinning particles. The biggest influence exists between the different experiment

444   classes i.e. particle sizes, which reveal different roughness and growth exponents that are on

445   the other hand very consistent within an individual class. But it has been demonstrated

446   (Renard et al., 2004; Schmittbuhl et al., 2004, Koehn et al., 2007), that these differences arise

447   from a transition from a surface energy dominated regime (where surface energies smoothen

448   the interface) to an elastic energy dominated regime (where elastic energies smoothen the

449   interface). The differences in the scaling exponents between the experimental classes are

450   therefore not caused by the heterogeneities themselves but by the processes that govern the

451   roughening on respective scales. We are thus convinced that the influence of the exact nature

452   of the heterogeneities plays a minor role and that roughening is dominated by an inherent

453   process that depends on the length-scale.

454   The quenched noise we introduced in the different simulations, i.e. changes in the dissolution

455   rate constant that influence the dissolution velocity of a particle (cp. Eq. 1), is a simple

456   chemical noise as pointed out by Koehn et al. (2007). We are aware that along natural

457   stylolitic interfaces the elastic parameters, surface energies, crystallographic orientations are

458   very likely to change, in addition to chemical variations. However the effects of a change of

459   these other parameters in our model also result in a change of the dissolution velocity. We

460   therefore argue that for the developing structure it should make no difference what the exact

461   nature of the noise is, since any particle with a slower dissolution velocity will pin the surface

462   and therefore cause a roughening of the interface.

463   It was demonstrated that individual natural stylolites from different outcrop localities and

464   lithologies, i.e. different host-rock compositions, reveal the same scaling behavior (e.g.

465   Renard et al., 2004; Schmittbuhl et al., 2004, Ebner et al., submitted). Consequently the

466   investigation of natural stylolites corroborates the fact that a common underlying mechanism

467   for stylolite roughening can be assumed rather than a roughening that is dominated by the

468   composition of the host rock.

469   Nevertheless we do not claim that knowledge of the exact nature or distribution of the

470   material heterogeneities is unimportant. Brouste et al., (2007) have shown that a changing

471   amount of heterogeneities might cause a stylolite to become a non-stationary signal with

472   alternating wavy and flat portions along the interface. We have not investigated the effects of

473   irregularly distributed noise since the heterogeneities are distributed equally in our model

474   setup.

475   The roughness data of simulated stylolites presented in this study reveal two self-affine

476   scaling regimes that are separated by a distinct crossover-length of $L\sim1.3$ mm, which is well

477   in line with investigations of natural stylolites (Renard et al., 2004; Schmittbuhl et al., 2004,

478   Ebner et al., submitted). Additionally we have detected a crossover in the growth of the

479   interface during which the initial growth exponent of $\beta\sim0.5$ up to a crossover interface width

480   of $w\sim1.23$ mm is replaced by a growth regime with an exponent of $\beta\sim0.8$. Due to the very

481   good correlation between the magnitudes of the crossover-length and the crossover interface

482   width we argue that both crossovers arise from the same process, namely the transitions from

483   a surface energy to an elastic energy dominated regime. The knowledge of the crossover

484   length L which can be derived from the finite pattern of a natural stylolite with the above

485   methods is thus equivalent to knowledge of the crossover interface width. This fact has

486   important consequences regarding the assessment of the amount of total compaction of

487   individual stylolites. Substituting the growth exponents and the compaction prefactors found

488   for the two growth regimes in combination with the crossover-length, which separates the two

489   growth regimes (cp. Fig. 10c), into Eq. 10 should allow an exact reconstruction of the amount

490   of total compaction from finite pattern of a natural stylolites.

491

492   **5. Conclusions**

493   In the course of this contribution we evaluated the scaling properties of simulated stylolites,

494   which facilitate a quantitative comparison with natural examples, exactly reproducing their

495   scaling. We observed only minor correlation between the exact nature of the noise introduced

496   in the model or the topography of the predefined interface and the scaling parameters

497   investigated, concluding that inherent processes i.e. the transition from a surface to an elastic

498   energy dominated regime control the roughening process.

499   Nevertheless the amount of heterogeneities has a negative effect on the maximum interface

500   width (w_{max}) achieved during deformation revealing increasing interface width with

501   decreasing amount of quenched noise. The absolute particle/noise size influences the

502   roughness and growth exponents, which in turn is caused by the transition from a surface to

503   an elastic energy dominated regime. Therefore it is important to know how large the noise or

504   pinning particles are in natural systems. The transition from surface energy as the dominant

505   stabilizing force of the interface to the dominance of elastic energies is the causation for the

506   most significant scaling transitions: (i) the roughness is characterized by two distinct spatial

507   scaling regimes on small and large length scales, respectively; (ii) the interface growth reveals

508   two growth regimes with a growth exponent of $\beta \sim 0.5$ up to a crossover interface width that

509   coincides with the crossover-length L followed by a growth regime with an exponent of $\beta \sim 0.8$

510   that eventually saturates due to finite size effects; (iii) the crossover interface width w

511   coincides with the crossover-length L and thus allows to accurately reconstruct the

512   compaction history of finite stylolite patterns.

513   Our study corroborates the evidence that the simple mechanisms summarized above support

514   analytical predictions and natural observations given in previous studies, and are a convincing

515   causation for the formation of stylolite roughness. However a detailed study on the exact

516   nature and distribution of quenched noise in the host rocks of natural stylolites would shed

517   light on the origin and initiation of these complex structures.

518

523

524   **References**

525   Barabasi, A. L. & Stanley, H. E. 1995. *Fractal concepts in surface growth*. Cambridge
526   University Press.
527   Bathurst, R. G. C. 1987. Diagenetically Enhanced Bedding in Argillaceous Platform
528   Limestones - Stratified Cementation and Selective Compaction. *Sedimentology* **34**(5),
529   749-778.
530   Bons, P. D. D., Koehn, D. & Jessell, M. W. 2008. Microdynamics Simulation. In: *Lecture
531   Notes in Earth Sciences* (edited by Friedmann, G. M. & Seilacher, A.) **106**. Springer,
532   Berlin, 406.
533   Brouste, A., Renard, F., Gratier, J. P. & Schmittbuhl, J. 2007. Variety of stylolites'
534   morphologies and statistical characterization of the amount of heterogeneities in the
535   rock. *Journal of Structural Geology* **29**(3), 422-434.
536   Buxton, T. M. & Sibley, D. F. 1981. Pressure Solution Features in a Shallow Buried
537   Limestone. *Journal of Sedimentary Petrology* **51**(1), 19-26.
538   Clark, S. P. J. 1966. *Handbook of Physical Constants*. Geological Society of America, New
539   York.
540   Dunnington, H. V. 1954. Stylolite development post-dates rock induration. *Journal of
541   sedimentary Petrology* **24**(1), 27-49.
542   Ebner, M., Koehn, D., Toussaint, R., Renard, F. & Schmittbuhl, J. submitted. Scaling of
543   natural stylolites and their use as stress-depth gauges. *Geophysical Research Letters.*

544 Fletcher, R. C. & Pollard, D. D. 1981. Anti-Crack Model for Pressure Solution Surfaces.
545   *Geology* **9**(9), 419-424.
546 Gratier, J. P., Muquet, L., Hassani, R. & Renard, F. 2005. Experimental microstylolites in
547   quartz and modeled application to natural stylolitic structures. *Journal of Structural*
548   *Geology* **27**(1), 89-100.
549 Guzzetta, G. 1984. Kinematics of Stylolite Formation and Physics of the Pressure-Solution
550   Process. *Tectonophysics* **101**(3-4), 383-394.
551 Hansen, A., Schmittbuhl, J., Batrouni, G. G. & de Oliveira, F. A. 2000. Normal stress
552   distribution of rough surfaces in contact. *Geophysical Research Letters* **27**(22), 3639-
553   3642.
554 Heald, M. T. 1955. Stylolites in Sandstones. *Journal of Geology* **63**(2), 101-114.
555 Katsman, R., Aharonov, E. & Scher, H. 2006. A numerical study on localized volume
556   reduction in elastic media: Some insights on the mechanics of anticracks. *Journal of*
557   *Geophysical Research-Solid Earth* **111**(B3), B03204.
558 Karcz, Z. & Scholz, C. H. 2003. The fractal geometry of some stylolites from the Calcare
559   Massiccio Formation, Italy. *Journal of Structural Geology* **25**(8), 1301-1316.
560 Koehn, D., Dysthe, D. K. & Jamtveit, B. 2004. Transient dissolution patterns on stressed
561   crystal surfaces. *Geochimica et Cosmochimica Acta* **68**(16), 3317-3325.
562 Koehn, D., Malthe-Sorenssen, A. & Passchier, C. W. 2006. The structure of reactive grain-
563   boundaries under stress containing confined fluids. *Chemical Geology* **230**(3-4), 207-
564   219.
565 Koehn, D., Renard, F., Toussaint, R. & Passchier, C. W. 2007. Growth of stylolite teeth
566   patterns depending on normal stress and finite compaction. *Earth and Planetary*
567   *Science Letters* **257**(3-4), 582-595.
568 Koehn, D., Ebner, M., Renard, F.,Toussaint, R. & Passchier C. W. in preparation. The use of
569   stylolites as paleo-stress-gauges.
570 Merino, E. 1992. Self-organization in stylolites. *American Scientist* **80**(5), 466.
571 Merino, E., Calas, A. & Fletcher, R. C. 2006. Genesis of self-organized zebra textures in
572   burial dolomites: Displacive veins, induced stress, and dolomitization. *Geologica Acta*
573   **4**(3), 383-393.
574 Park, W. C. & Schot, E. H. 1968. Stylolites: their nature and origin. *Journal of sedimentary*
575   *Petrology* **38**(1), 175-191.
576 Railsback, L. B. 1993. Lithologic Controls on Morphology of Pressure-Dissolution Surfaces
577   (Stylolites and Dissolution Seams) in Paleozoic Carbonate Rocks from the Mideastern
578   United-States. *Journal of Sedimentary Petrology* **63**(3), 513-522.
579 Railsback, L. B. 1998. Evaluation of spacing of stylolites and its implications for self-
580   organizations of pressure dissolution. *Journal of Sedimentary Research* **68**(1), 2-7.
581 Renard, F., Schmittbuhl, J., Gratier, J. P., Meakin, P. & Merino, E. 2004. Three-dimensional
582   roughness of stylolites in limestones. *Journal of Geophysical Research-Solid Earth*
583   **109**(B3), -.
584 Rutter, E. H. 1983. Pressure solution in nature, theory and experiment. *Journal of the*
585   *Geological Society of London* **140**(5), 725-740.
586 Schmittbuhl, J., Vilotte, J. P. & Roux, S. 1995. Reliability of Self-Affine Measurements.
587   *Physical Review E* **51**(1), 131-147.
588 Schmittbuhl, J., Renard, F., Gratier, J. P. & Toussaint, R. 2004. Roughness of stylolites:
589   Implications of 3D high resolution topography measurements. *Physical Review Letters*
590   **93**(23), -.
591 Simonsen, I., Hansen, A. & Nes, O. M. 1998. Determination of the Hurst exponent by use of
592   wavelet transforms. *Physical Review E* **58**(3), 2779-2787.
593 Stockdale, P. B. 1922. Stylolites: their nature and origin. *Indiana University Studies* **9**, 1-97.

594 Tada, R. & Siever, R. 1989. Pressure Solution during Diagenesis. *Annual Review of Earth and*
595   *Planetary Sciences* **17**, 89-118.
596

597 **Figure captions**

598

599 **Figure 1**: Plane section of a bedding parallel stylolite in a jurassic limestone from Cirque de

600 Navacelles (southern France). The rough interface is accentuated by a thin clay layer that is

601 considered to be the residuum of the dissolved rock mass.

602

603 **Figure 2:** Simplified sketch of the setup of the numerical model (modified after Koehn et al.,

604 2007).The top and bottom walls of the box are moved inwards simultaneously to stress the

605 system and initiate dissolution along the interface. **a)** Initial configuration of the setup

606 showing a flat interface (dashed line). **b)** Configuration after a certain amount of compaction.

607 The interface (dashed line) has developed a distinct roughness, note that the heterogeneities

608 (darker spheres) accumulate along the interface.

609

610 **Figure 3:** Growth of three stylolites with similar heterogeneities but different lengths and

611 discretization resolution. Left panels show 3D plots of the stylolite growth from a flat

612 interface until the end of the experiment. Right panels show 3 individual deformation steps

613 (step 400, 2000 & 4000) corresponding to the solid lines in the 3D plot **a)** surface class (box

614 size=0.4 cm) **b)** intermediate class (box size =4 cm) **c)** elastic class (box size =40 cm); Notice

615 the disrupted growth of the surface class whereas the elastic class exhibits very continuous

616 growth and pronounced peaks and teeth.

617

618 **Figure 4:** Roughness characterization of single deformation steps by means of the Hurst

619 exponent. **a)** 1D profile (deformation step 3000) of the surface class with 5% pinning particles

620 and a dissolution rate constant of k=0.4; **b)** Fourier power spectrum $P(k)$ of the signal from

621   Fig. 4a plotted as a function of the wavenumber k. Linear regression (solid line) is calculated

622   from the binned spectra (crosses), the slope of the regression is a function of the Hurst

623   exponent, see section 3.1.1. for detailed description. **c)** Wavelet spectra $W(a)$ plotted (crosses)

624   as a function of the scaling parameter a (see average wavelet coefficient-method in section

625   3.1.1.). The slope of the linear regression (solid line) is again a function of the Hurst

626   exponent. **d)** Evolution of the Hurst exponent in the course of an entire experiment for the

627   Fourier and AWC methods. Stars indicate the Hurst exponent of the 1D signal shown in Fig.

628   4a for the two methods used. Notice the leveling off at a specific Hurst exponent (plateau

629   value) which is characteristic for all simulations.

630

631

632   **Figure 5:** Composite plots showing the roughness data (Hurst exponents) for the surface and

633   elastic classes. **a)** Hurst exponent plotted versus dissolution rate constants k with a fixed

634   amount of pinning particles of 5% (where $k=1$ is the dissolution rate of the matrix). **b)** Hurst

635   exponent plotted versus amount of pinning particles with a dissolution rate constant of $k=0.5$

636   for all experiments. The error bars correspond to the standard deviation given by the

637   fluctuation around the plateau values, compare Fig 4d.

638

639   **Figure 6:** Interface growth depicted by means of the interface width (Eq. 8). **a)** Log-log plot

640   of the interface width as a function of time in the surface class (5% pinning particles &

641   dissolution rate constant of 0.4). Growth exponent $\beta=0.5$ is given by the slope of the linear

642   regression (solid line). Notice the saturation point (indicated by arrow) i.e. interface width

643   remains constant during ongoing deformation. **b)** Log-log plot of the interface width as a

644   function of time in the elastic class (5% pinning particles & dissolution rate constant of 0.4).

645   Notice the two successive growth regimes characterized by an initial growth exponent of

646    $\beta=0.5$ up to a crossover width (indicated by arrow) followed by an exponent of $\beta=0.8$; no

647 saturation can be observed within the given simulation time. **c)** Proposed composite graph of

648 the interface growth of simulated stylolites. Two successive growth regimes separated by a

649 narrow crossover width that are dominated either by surface or elastic energies are followed

650 by a saturation of the interface growth due correlation introduced by finite size effects.

651

652 **Figure 7:** Total compaction displacement expressed as a linear function (solid line) of the

653 interface width and the compaction prefactor (compare Eq. 10). **a)** Surface class experiment

654 (5% pinning particles & dissolution rate constant of $k=0.4$) demonstrates that the relationship

655 is only valid as long as the interface is not saturated i.e. strong deviation from linear trend

656 (compare Fig 6a). **b)** Elastic class experiment (5% pinning particles & dissolution rate

657 constant of 0.4) reveals an accurate reproduction of the linear relationship (solid line) stated in

658 Eq. 10. No saturation was observed in the given simulation time.

659

660 **Figure 8:** Cumulative data for the surface, intermediate and elastic classes for: **a)** Growth

661 exponent versus dissolution rate constant (pinning particles fixed at 5%); **b)** Growth exponent

662 versus amount of pinning particles (dissolution rate constant fixed at $k=0.5$); **c)** Compaction

663 prefactor versus dissolution rate constant (pinning particles fixed at 5%); **d)** Compaction

664 prefactor versus amount of pinning particles (dissolution rate constant fixed at $k=0.5$).

665 Maximum interface width normalized by the particle size attained during experimental runs

666 for the *surface*, *intermediate* and *elastic* class **e)** with changing dissolution rate constant (with

667 5% pinning particles); **f)** with changing amount of pinning particles (dissolution rate constant

668 is fixed at 0.5).

669

670 **Figure 9:** The influence of the topography of the initial predefined interface on the dynamic

671 roughness evolution. **a)** Rough initial interface used as starting point to evaluate the interface

672 width evolution on top of this roughness for a *surface class* simulation with 5% pinning

673   particles and a pinning factor of 0.5 (for details see text). **b)** Comparison of the interface

674   width evolution of an initially flat and rough (see Fig 9a) interface. Both interfaces show a

675   similar evolution with growth exponents of 0.54 and 0.51 for the flat and rough initial

676   interface respectively. Notice that both growth and the roughness exponents (not shown) are

677   independent of the initial topography of the predefined interface.

678

679   **Figure 10:** Crossover phenomena in the roughness scaling and interface growth. **a)** 1D signal

680   of an experiment from the intermediate class (5% pinning particles; dissolution rate constant

681    $k=$ 0.4); **b)** Fourier power spectrum (inset) of the signal and binned spectra (crosses). A

682   nonlinear model function (for explanation see text) used to minimize the original data (solid

683   line) is used to accurately locate the position of the crossover length (triangle) $L=$ 1.27 mm; **c)**

684   Log-log plot of the interface width versus time of the elastic class (5% pinning particles &

685   dissolution rate constant $k=0.4$). Notice the two successive growth regimes characterized by

686   an initial growth exponent of $\beta=0.5$ up to a crossover width $w=1.24$ mm followed by an

687   exponent of $\beta=0.8$. Notice that both crossover scales correspond to the transition from a

688   surface to an elastic energy dominated regime.

689

690   **Figure 11:** Crossover length L and crossover interface width w plotted as a function of the

691   quenched noise. **a)** Crossover length (circles) calculated from the Fourier power spectrum (cp.

692   Fig. 10b) and crossover interface width (diamonds) for simulations with different dissolution

693   rate constants. **b)** Crossover length (circles) and crossover interface width (diamonds) for

694   simulations with different amounts of pinning particles.

695

Figure 1
Click here to download high resolution image
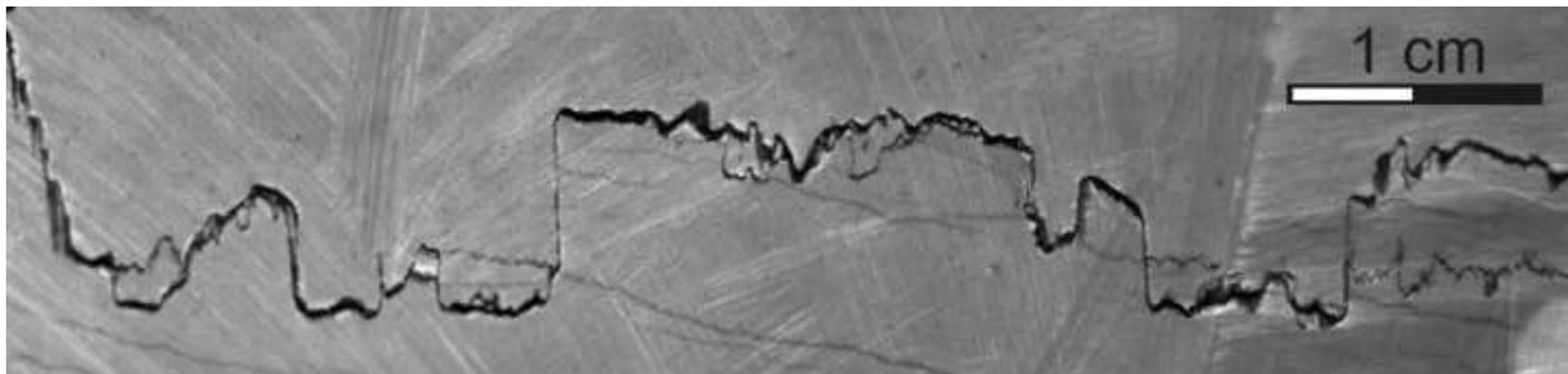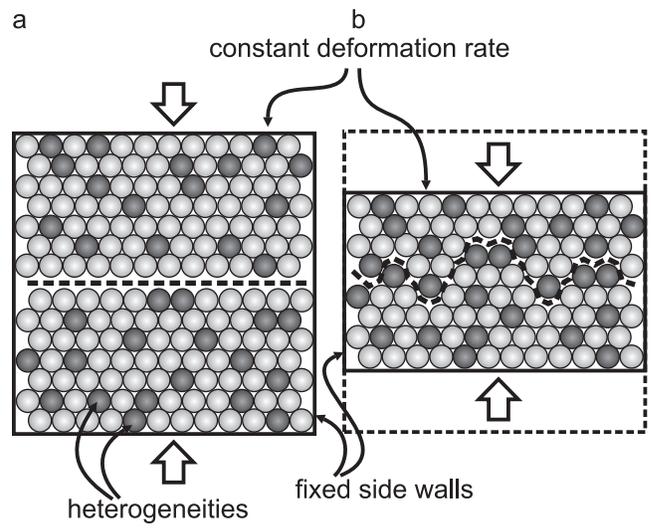
Figure 1

Figure 2
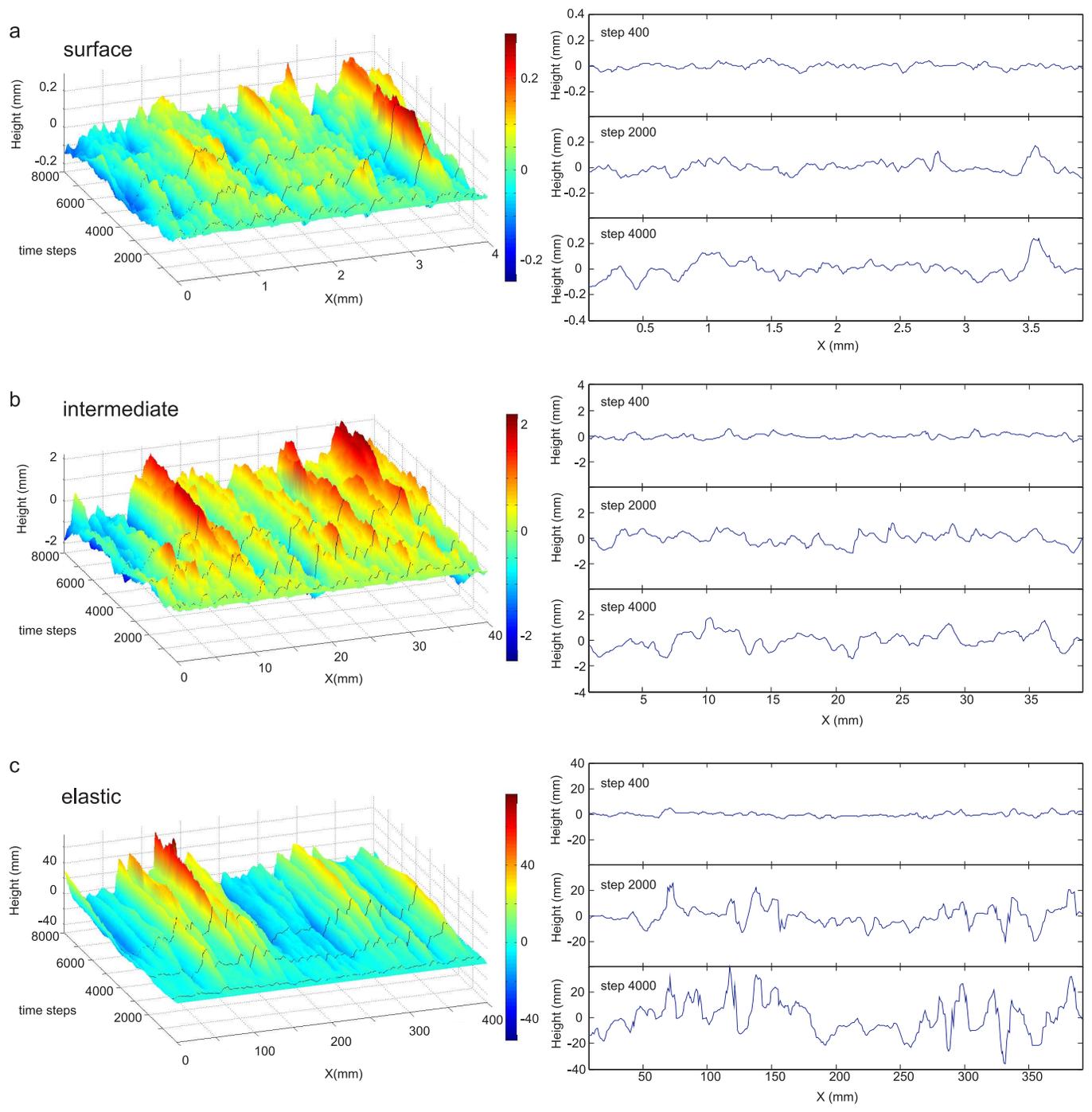
Figure 2

Figure 3

Figure 3

Figure 4
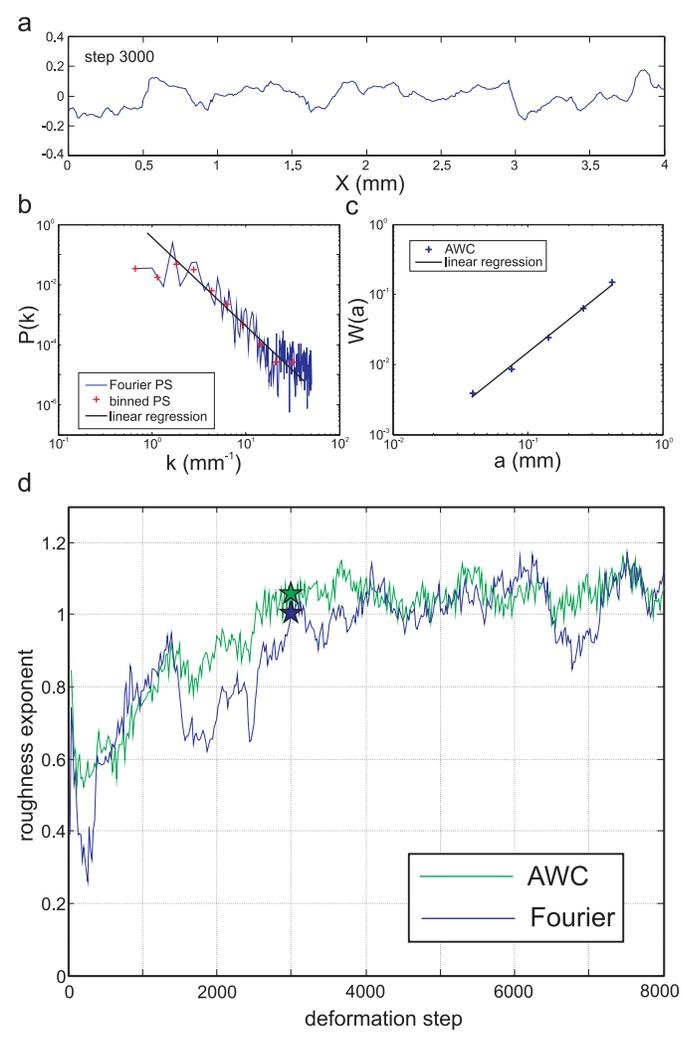
Figure 4

Figure 5
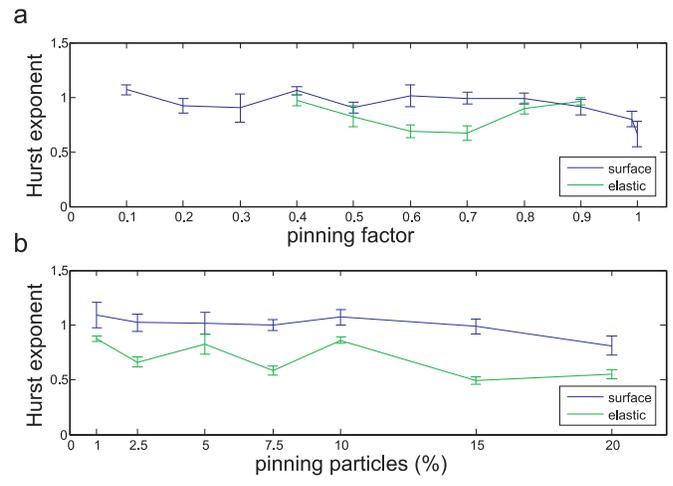
Figure 5

Figure 6
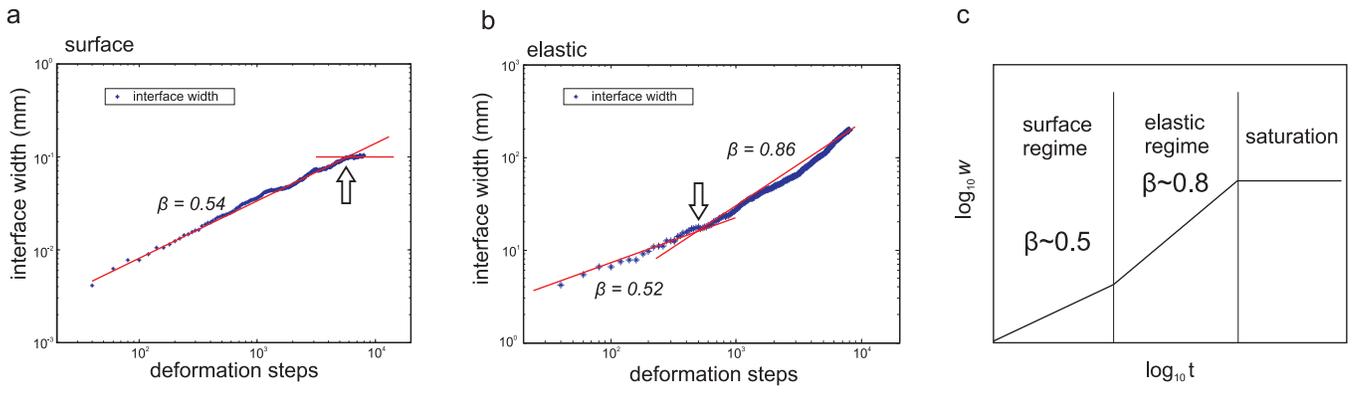
Figure 6

Figure 7
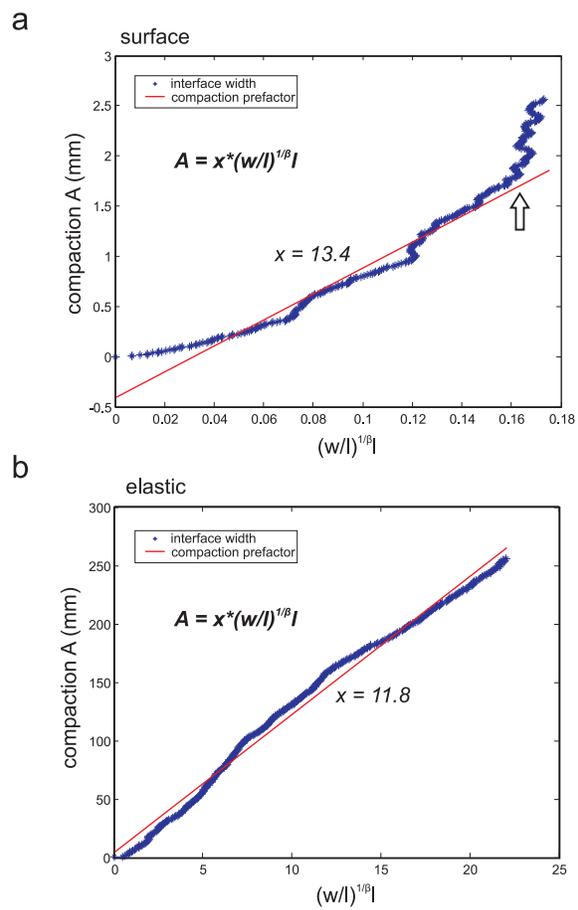
Figure 7

Figure 8

Figure 8

Figure 9

a

b
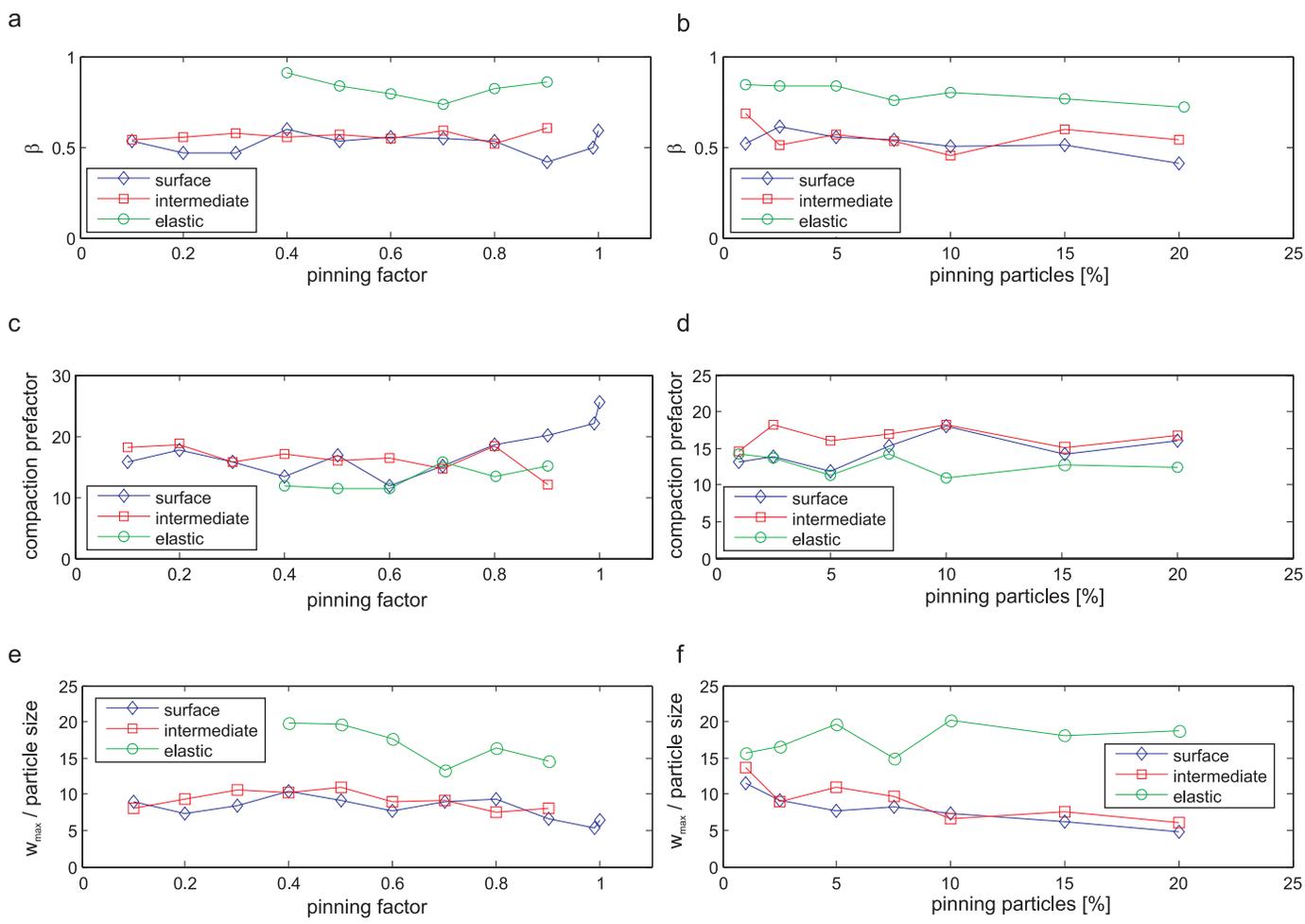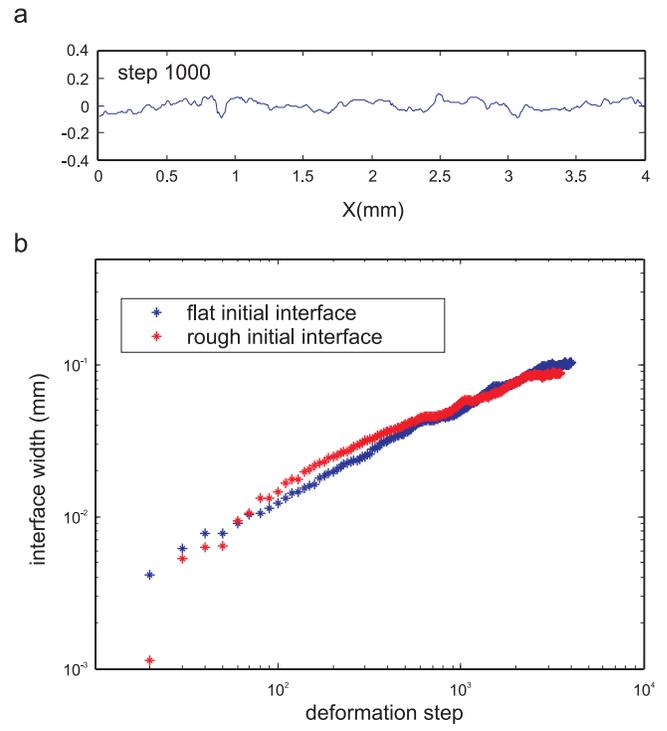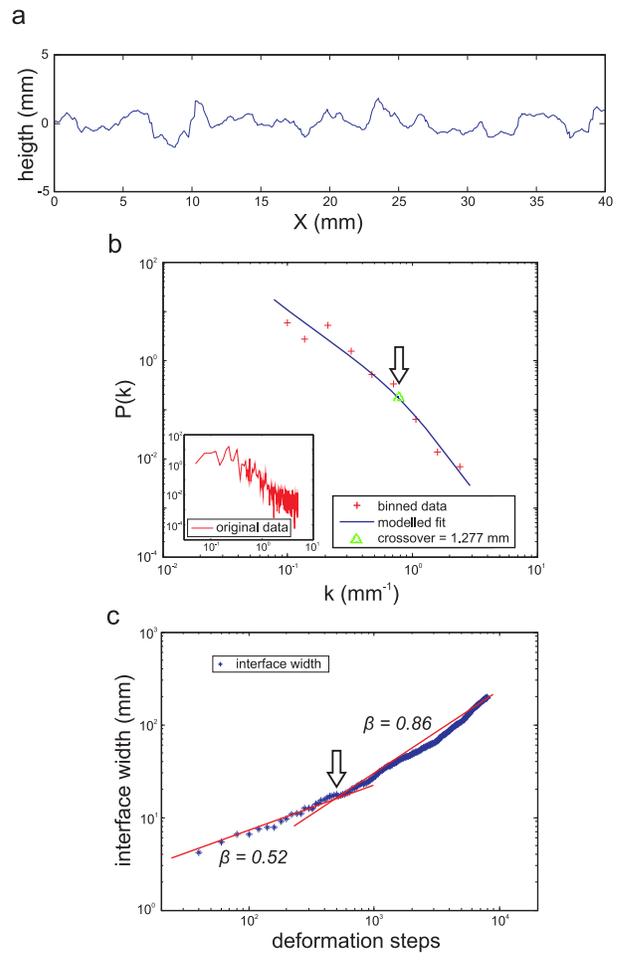
Figure 9

Figure 10

Figure 10

Figure 11

Figure 11